

# Facile Transfer Hydrogenation of N-Heteroarenes and Nitroarenes Using Magnetically Recoverable Pd@SPIONs Catalyst

Huda S. Alghamdi, Afnan M. Ajeebi, Md. Abdul Aziz, Atif Saeed Alzahrani, and M. Nasiruzzaman Shaikh\*



Cite This: *ACS Omega* 2024, 9, 11377–11387



Read Online

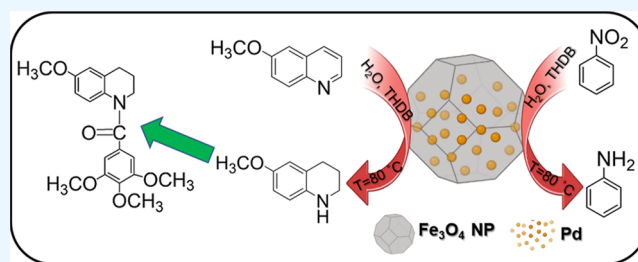
ACCESS |

Metrics & More

Article Recommendations

Supporting Information

**ABSTRACT:** Catalysts with active, selective, and reusable features are desirable for sustainable development. The present investigation involved the synthesis and characterization of bear-surfaced ultrasmall Pd particles (<1 nm) loaded onto the surface of magnetic nanoparticles (8–10 nm). The amount of Pd loading onto the surface of magnetite is recorded as 2.8 wt %. The characterization process covered the utilization of scanning electron microscopy (SEM), energy-dispersive spectroscopy (EDS), transmission electron microscopy (TEM), inductively coupled plasma (ICP), and X-ray photoelectron spectroscopy (XPS) methods. The Pd@Fe<sub>3</sub>O<sub>4</sub> catalyst has shown remarkable efficacy in the hydrogenation of quinoline, resulting in the production of >99% N-ring hydrogenated (py-THQ) product. Additionally, the catalyst facilitated the conversion of nitroarenes into their corresponding aniline derivatives, where hydrogen was achieved by H<sub>2</sub>O molecules with the aid of tetrahydroxydiboron (THDB) as an equilibrium supportive at 80 °C in 1 h. The high efficiency of a transfer hydrogenation catalyst is closely related to the metal–support synergistic effect. The broader scope of functional group tolerance is evaluated. The potential mechanism underlying the hydrogenation process has been elucidated through the utilization of isotopic labeling investigations. The application of the heterocyclic compound hydrogenation reaction is extended to formulate the medicinally important tubular polymerization inhibitor drug synthesis. The investigation of the recyclability of Pd@Fe<sub>3</sub>O<sub>4</sub> has been conducted.



## INTRODUCTION

1,2,3,4-Tetrahydroquinoline (py-THQ) derivatives are privileged structures in the pharmaceutical industry for the preparation of a series of medicinal antibacterial agents, such as flumequine,<sup>1,2</sup> torcetrapib,<sup>3</sup> tubulin polymerization inhibitor,<sup>4</sup> AChE inhibitor,<sup>5</sup> and the antiarrhythmic drug nicanoprol.<sup>6,7</sup> Producing these moieties is important and has received a great deal of attention in recent years due to their widespread use. py-THQ derivatives are typically synthesized by the direct hydrogenation of quinoline, a method that is widely regarded as the most convenient and promising approach owing to its high atom efficiency.<sup>8</sup> However, the process of quinoline hydrogenation ideally encompasses the production of 5,6,7,8-tetrahydroquinoline (bz-THQ) and decahydroquinoline (DHQ), alongside py-THQ.<sup>9</sup> Therefore, the achievement of selective synthesis of the hydrogenated pyridine ring product py-THQ with a more benign approach is a challenging task. In this context, numerous outstanding homogeneous catalytic systems, such as Fe,<sup>10</sup> Co,<sup>11,12</sup> Rh,<sup>13</sup> Ir,<sup>14</sup> Pt,<sup>15</sup> and Pd,<sup>16</sup> have been developed with excellent performance in hydrogenation reactions. Despite the increased activity and selectivity, the difficulties in recovering the catalysts, ligands, and metals after the reaction make such catalytic systems less affordable. Furthermore, they lack the

ecological economics feature due to the extensive use of toxic organic solvents during the catalyst preparation steps. Hence, their broad commercialization efforts are constrained.<sup>17,18</sup>

Consequently, catalyst immobilization gains importance because of the ease of preparation, recovery, and reuse for multiple consecutive cycles. In addition, separation of the catalyst by simple filtration, precipitation, or centrifugation can be achieved. Therefore, many heterogeneous systems have been developed for the hydrogenation of unsaturated compounds, especially quinoline. For instance, Wei et al. demonstrated N-doped graphene-coated cobalt nanoparticle catalysts for the efficient hydrogenation of quinoline.<sup>19</sup> When rhodium nanoparticles (RhNPs) are immobilized in a Lewis-acidic ionic liquid (IL) structure, the heteroaromatic ring hydrogenated product from quinoline works very well as demonstrated by Karakulina et al.<sup>20</sup> Amphiphilic mesoporous cocatalysts, Co@Co–N–C@SBA-15, are used to hydrogenate

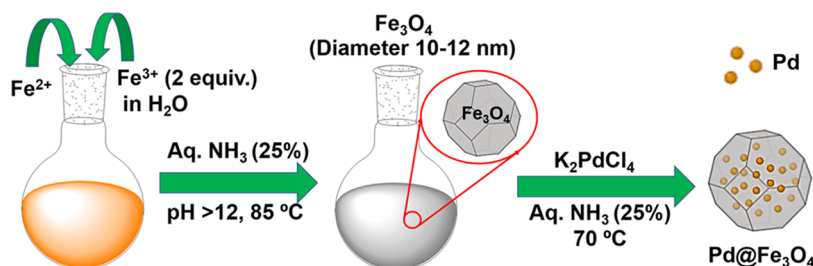
**Received:** September 29, 2023

**Revised:** February 4, 2024

**Accepted:** February 9, 2024

**Published:** March 1, 2024



Scheme 1. Preparation of the Catalyst Pd@Fe<sub>3</sub>O<sub>4</sub>

the nitroarenes compounds.<sup>21</sup> However, most of them use molecular hydrogen, which is challenging to handle due to its higher flammability and requires the use of specialized high-pressure equipment.<sup>22</sup> Therefore, a facile, cost-effective, and more environmentally benign hydrogenation procedure is anticipated. In this context, catalytic transfer hydrogenation (CTH) procedure is a safer, cleaner, and more efficient process for reducing a series of unsaturated compounds that can be reduced using sacrificial hydrogen donors, such as formic acid (HCOOH), hydrazine hydrate (NH<sub>2</sub>NH<sub>2</sub>·H<sub>2</sub>O), ammonia borane (NH<sub>3</sub>·BH<sub>3</sub>), and sodium borohydride (NaBH<sub>4</sub>).<sup>23,24</sup> In line with this effort, numerous catalytic systems have been developed, and most of the CTH systems have shown excellent results. For example, El kadiri et al. demonstrated that bismuth nanoparticles (BiNPs) supported the chitosan biopolymer (Bi@CS) catalyst for the selective and controlled reduction of nitroaromatic compounds to anilines and azoarenes using NaBH<sub>4</sub> in water.<sup>25</sup> Recently, Zhou et al. reported the catalytic transfer hydrogenation of nitro compounds into amines over graphene oxide-supported Pd nanoparticles.<sup>26</sup>

Judicious choice of support plays a crucial role in affecting the metal–support interaction, which leads to substantial changes in the activity and selectivity of the catalyst. In this context, iron oxide nanoparticles have emerged as outstanding and promising solid support materials due to their abundant availability, easy preparation techniques, lack of toxicity, chemical stability, and ease of separation by an external magnet.<sup>27</sup> In addition, there is a massive prospect for enhancing the active catalytic sites when transformed from bulk to the nanosized regime (<10 nm).<sup>28</sup> Even though only a few heterogeneously functionalized metal catalysts, such as Pd, Ru, or Rh, on various supports are currently available for the hydrogenation of quinoline and nitroarene, extreme reaction conditions are needed to fully convert quinoline to py-THQ or nitroarene to aniline using heterogeneous catalysts.

In this regard, as a part of our continuous efforts, palladium nanoparticles supported on magnetite, as shown in Scheme 1 have been developed for the transfer hydrogenation of quinoline and nitroarene compounds in an aqueous medium using tetrahydroxydiboron (THDB) as a sacrificial agent. A possible mechanism of transfer hydrogenation has been proposed. The reusability of the catalyst is presented. Also, this study has been extended to the preparation of quinoline-based tubular polymerization inhibitors using the above hydrogenation catalyst.

## EXPERIMENTAL SECTION

**Materials and Methods.** All chemicals were purchased from Sigma-Aldrich and used as received. All experiments utilized deionized water (18.2 M specific conductivity). For Fourier transform infrared (FTIR), KBr was used as the

infrared (IR) transparent window material on the Nicolet 720, which has a wavenumber range of 500–4000 cm<sup>-1</sup>. X-ray diffraction (XRD) data were acquired using a Rigaku Ultima-IV diffractometer and Cu–K radiation (1.5405) at 40 kV and 25 mA over a 2θ range from 5 to 90°. Samples for scanning electron microscopy (SEM) were fabricated from ethanolic solutions on alumina stubs and gold-coated using an automatic gold coater (Quorum, Q150T E). For elemental analysis and mapping, energy-dispersive X-ray spectra (EDS) were produced using a Lyra 3 attachment to the SEM. Operating transmission electron microscopy (TEM), a JEOL JEM2100F transmission electron microscope, was utilized to acquire TEM pictures. The TEM samples were prepared by dropping them from an ethanolic suspension onto a copper plate at room temperature and allowing them to dry. Using inductively coupled plasma optical emission spectrometry, the quantity of Pd@Fe<sub>3</sub>O<sub>4</sub> nanoparticles in the catalyst was determined (inductively coupled plasma optical emission spectrometry (ICP-OES); PlasmaQuant PO 9000-Analytik Jena). Initially, the catalyst samples were digested in a diluted mixture of HNO<sub>3</sub> and HCl. Using standard solutions generated calibration curves for palladium (ICP Element Standard solutions, Merck). The surface composition and oxidation states were measured using an X-ray photoelectron spectrometer (XPS), an X-ray monochromator with Al–K microfocusing, and an X-ray monochromator (ESCALAB 250Xi XPS Microprobe, Thermo Scientific). Magnetic susceptibilities were determined at room temperature using a SQUID equipped with a 7 T magnet with a temperature range of 1.8–400 K in KAUST, Saudi Arabia. A multiphase (10-place) Teflon-capped parallel reactor equipped with a magnetic stirrer (STEM, Electrothermal, Serial No. M433640) was used to carry out the catalytic reactions in water. In addition to mass fragmentation detection, a Shimadzu 2010 Plus gas chromatograph combined with a mass spectrometer (GC-MS, Japan) was used to identify catalytic products by comparing the species to those in the Wiley Registry Mass Spectral Library and identifying them based on their molecular ion (M<sup>+</sup>). A Bruker Advance 400 spectrometer was used for the <sup>1</sup>H and <sup>13</sup>C solution NMR experiments. <sup>1</sup>H and <sup>13</sup>C NMR chemical shifts were given as δ values with reference to tetramethylsilane (TMS) as an internal standard.

**Synthesis of Fe<sub>3</sub>O<sub>4</sub> Catalyst.** The magnetic nanoparticles of Fe<sub>3</sub>O<sub>4</sub> in sizes 8–10 nm were prepared by the coprecipitation method as described elsewhere.<sup>17</sup> First, Fe(NO<sub>3</sub>)<sub>2</sub>·4H<sub>2</sub>O (2 g, 10 mmol) and Fe(NO<sub>3</sub>)<sub>3</sub>·9H<sub>2</sub>O (8 g, 20 mmol) were dissolved in 200 mL of deionized water in a round-bottom flask with a continuous stirring speed of 500 rpm, and the vessel was flushed with the argon. Then, the mixture was heated at 85 °C in an oil bath for 30 min until the solution became clear. Subsequently, 60 mL of aqueous

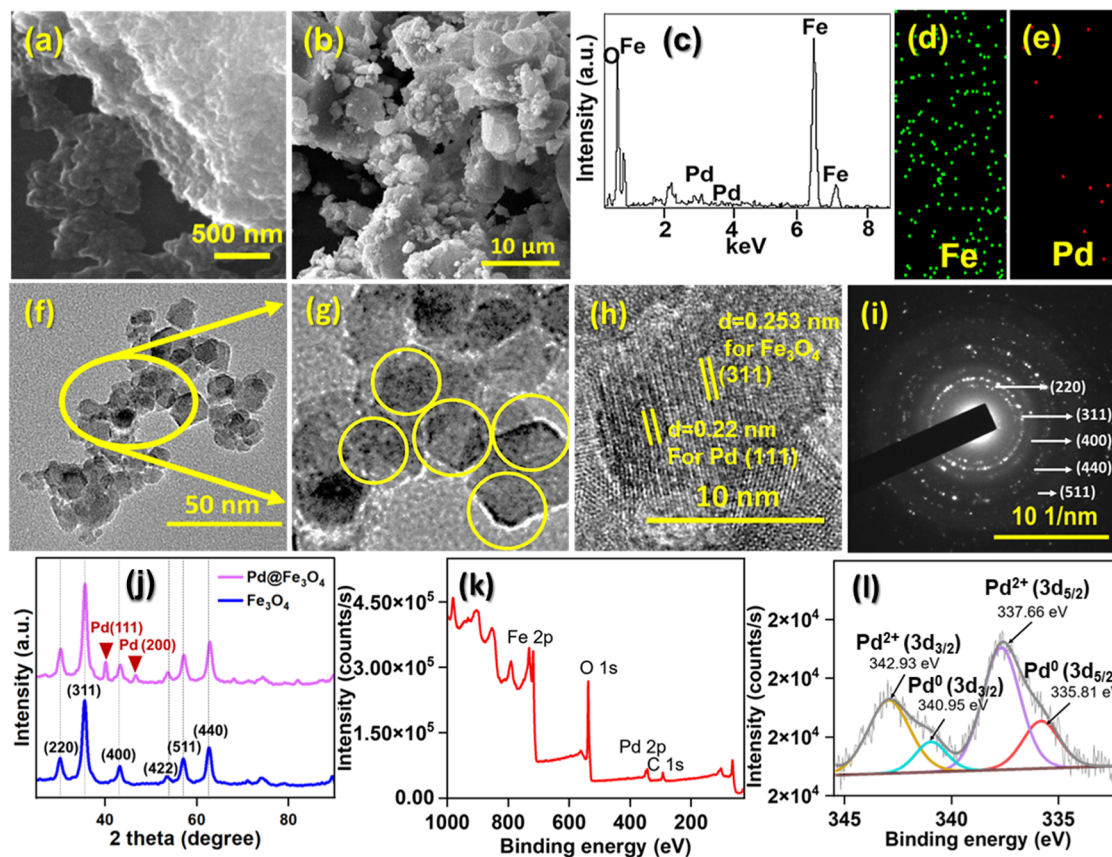


**Figure 1.** Illustration of the SEM images of (a) pure  $\text{Fe}_3\text{O}_4$  and (b)  $\text{Pd@Fe}_3\text{O}_4$ ; (c) EDX of  $\text{Pd@Fe}_3\text{O}_4$ ; elemental mapping of (d) Fe and (e) Pd; (f) TEM image of pure magnetite; (g) magnified TEM image of Pd-decorated  $\text{Fe}_3\text{O}_4$ ; (h) HRTEM image of  $\text{Pd@Fe}_3\text{O}_4$  (i) SAED pattern of  $\text{Pd@Fe}_3\text{O}_4$ ; (j) XRD pattern of  $\text{Pd@Fe}_3\text{O}_4$ ; (k) survey (l) Pd oxidation states.

ammonia (25%) was added to the mixture to raise the pH to 12 and maintain the alkaline pH for 2 h by the periodic addition of an aqueous solution of ammonia. Thereafter, the solution's color was changed from orange to black. The black solid was collected by using a simple magnet at the bottom of the flask to decant the colorless solution. The black slurry was washed with fresh deionized water ( $3 \times 25$  mL) to eliminate the unreacted iron precursors and nonmagnetic materials, if any, by holding a magnet at the bottom of the vessel. The sample was collected and dried for 12 h under a vacuum. The black-color magnetic powdered materials were used for further characterization.

**Synthesis of  $\text{Pd@Fe}_3\text{O}_4$  Catalyst.** In a round-bottom flask, freshly prepared magnetic nanoparticles (700 mg) were ground in a mortar pestle, suspended in 30 mL of ethanol, and then sonicated for about 30 min using a bath sonicator. Then, a solution of potassium tetrachloropalladate ( $\text{K}_2\text{PdCl}_4$ ) (150 mg) in deionized (DI) water (30 mL) was added to the  $\text{Fe}_3\text{O}_4$  suspension under an inert gas atmosphere. The mixture was heated using an oil bath at  $70^\circ\text{C}$  and continued stirring for 3 h for uniform decoration. Afterward,  $\text{K}_2\text{PdCl}_4$  was reduced using aqueous ammonia (15 mL). The mixture was stirred for another 12 h at the same temperature. The resultant precipitate was collected by putting a simple magnet in it and washed with deionized water ( $4 \times 15$  mL) to remove any undecorated Pd precursor. The final magnetic material ( $\text{Pd@Fe}_3\text{O}_4$ ) was vacuum-dried for 12 h and used for the catalytic transfer hydrogenation reactions.

### Procedure for Quinoline Hydrogenation Using $\text{Pd@Fe}_3\text{O}_4$ Catalyst.

Quinoline and its derivatives were hydrogenated by the transfer hydrogen (TH) reaction, using water as a green solvent. The experiments were conducted in a Teflon-capped 10 mL glass reaction tube placed in a reactor, which is capable of running 10 parallel reactions simultaneously. The conditions were as follows: quinoline (0.5 mmol, 59  $\mu\text{L}$ ),  $\text{Pd@Fe}_3\text{O}_4$  catalyst (5 mg), and 10 mL of deionized water were added into a reaction tube. Then, THDB (2 mmol, 179 mg) was added to the suspension and stirred at  $80^\circ\text{C}$  with a stirring speed of 250 rpm. The progress of the reaction was monitored by thin-layer chromatography (TLC) and gas chromatography–mass spectrometry (GC-MS). After completion of the reaction, the product was extracted with chloroform ( $3 \times 5$  mL), combined with organic layers, dried with sodium sulfate, and then filtered through a short column packed with silica gel. The product was taken up for GC to measure the conversion and selectivity and identified by its molecular ion peak ( $m/z$ ) detected in GC-MS.

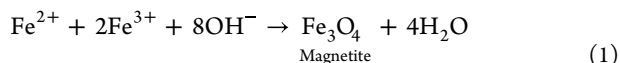
### Procedure for Nitroarene Hydrogenation Using $\text{Pd@Fe}_3\text{O}_4$ Catalyst.

By employing water as a green solvent in the TH reaction, nitroarene and its derivatives were hydrogenated. The catalytic reactions were carried out in the same 10-place parallel reactor. The conditions were as follows: nitrobenzene (0.5 mmol, 50.83  $\mu\text{L}$ ),  $\text{Pd@Fe}_3\text{O}_4$  catalyst (5 mg), and 10 mL of deionized water were placed in a reaction tube with continuous stirring. THDB (2 mmol, 179 mg) was added at  $80^\circ\text{C}$ . The reaction was monitored by TLC, GC-MS, and UV. Then, the product was extracted 3 times in 5 mL of chloroform

(3 × 5 mL), combined with the organic layers, dried with sodium sulfate, and then filtered through a short column filled with silica gel. The conversion and selectivity were measured by GC, and the products were identified by GC-MS with the appearance of their corresponding molecular ion peak (*m/z*) in mass spectra.

## RESULTS AND DISCUSSION

**Synthesis of Pd@Fe<sub>3</sub>O<sub>4</sub> Composite.** An aqueous solution containing Fe<sup>2+</sup> and Fe<sup>3+</sup> (Fe<sup>2+</sup>/Fe<sup>3+</sup> = 1:2 molar ratio), was reduced by aqueous NH<sub>3</sub>, forming highly aggregated black-colored magnetic nanoparticles eq 1.<sup>17,29,30</sup>



The stretching frequency at 586 cm<sup>-1</sup> for the Fe–O bond in the FTIR data confirms the formation of the pure phase of magnetite (Supporting Information, Figure S1). In addition, the red shift of the peak at 1630 cm<sup>-1</sup> observed may be due to surface stress during the decoration process.<sup>31</sup> Raman studies were used to confirm the purity of the magnetite, and the results showed that the characteristic bands at 667 and 536 cm<sup>-1</sup> are associated with the A<sub>1g</sub> and T<sub>2g</sub> transition, ensuring the exclusive formation of Fe<sub>3</sub>O<sub>4</sub> nanocrystals by excluding the presence of moderately magnetic of γ-Fe<sub>2</sub>O<sub>3</sub> phase in bulk (Figure S2).<sup>32,33</sup>

To obtain the maximum exposed surface for Pd nanoparticle decoration, the magnetic nanoparticle suspension in chloroform was vigorously sonicated. Then, the Pd metal loading capacity was optimized by adding various amounts of Pd metal precursors (K<sub>2</sub>PdCl<sub>4</sub>). Initially, 7 wt % of the Pd equivalent to 150 mg of K<sub>2</sub>PdCl<sub>4</sub> was added, and the actual Pd metal content was recorded as 2.8 wt %, which was measured by inductively coupled mass spectrometry integrated with optical emission spectrometry (ICP-OES). As the metal loading increased from 7 to 15 wt %, the Pd content remained almost constant, as the ICP-OES data show, indicating the surface loading saturation (Table S1). This information is well supplemented by the elemental mapping of Fe and Pd (Figure 1d,e).

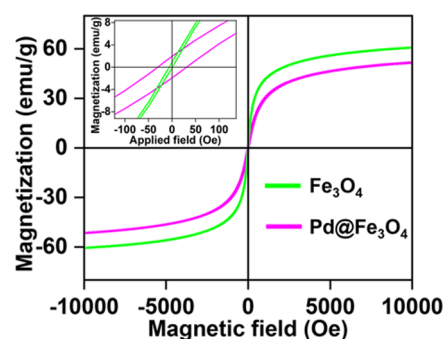
Figure 1a,b shows field emission SEM (FESEM) images highlighting the shape, size, and homogeneity of pure Fe<sub>3</sub>O<sub>4</sub> and Pd@Fe<sub>3</sub>O<sub>4</sub>. SEM shows the spherical-shaped particles with a uniform size distribution of the Pd@Fe<sub>3</sub>O<sub>4</sub> composite material. The energy-dispersive X-ray (EDX) results exhibited the existence of the Pd element in the Pd@Fe<sub>3</sub>O<sub>4</sub> composite (Figure 1c) and their homogeneous distribution all over the Fe<sub>3</sub>O<sub>4</sub> surface, which was detected by confined area elemental mapping (Figure 1d,e). TEM images (Figure 1f,g) show well-dispersed Pd@Fe<sub>3</sub>O<sub>4</sub> particles with a narrow size distribution in the 8–10 nm diameter range, which was further plotted by the size distribution (8.6 nm) curve (Figure S3). The TEM detected the decoration of the ultrasmall Pd particles (<1 nm) as small dots on the surface of magnetite (Figure 1g). These data were well supplemented during the elemental mapping of Pd@Fe<sub>3</sub>O<sub>4</sub> (Figure 1d,e). This ultrasmall Pd nanoparticle formation could be due to the increase in surface potential (Figure S4), which led to a decrease in the size of the Pd particles in the subnano range during the decoration process.<sup>34,35</sup> The crystalline nature of the Pd@Fe<sub>3</sub>O<sub>4</sub> (Figure 1h) was further confirmed by high-resolution TEM (HRTEM), which proved the lattice spacing *d*-value of 2.35 Å, corresponding to the cubic spinel structure of Fe<sub>3</sub>O<sub>4</sub>. The selected area electron diffraction (SAED) showed reflections of

0.223 Å that were attributed to the ⟨111⟩ plane of the subnanometric Pd particles, as shown in Figure 1i.<sup>36,37</sup>

The XRD signature patterns of Fe<sub>3</sub>O<sub>4</sub> and the catalyst, Pd@Fe<sub>3</sub>O<sub>4</sub>, are shown in Figure 1j. The X-ray diffraction pattern of pure magnetic nanoparticles (Fe<sub>3</sub>O<sub>4</sub>) displays well-defined broad peaks at 2θ = 30.22, 35.70, 41.10, 53.40, 57.10, and 63.20° with relatively high intensity, indicating a higher order of crystallinity with the spinel cubic structure where Fe<sup>3+</sup> is positioned in octahedral sites (card no. 00–005–0681; Figure S5a). In contrast, Fe<sup>2+</sup> occupies the tetrahedral (Td) position, as Fe<sub>3</sub>O<sub>4</sub> contains an equal amount of Fe<sup>3+</sup> and Fe<sup>2+</sup>.<sup>38</sup> However, the XRD of Pd@Fe<sub>3</sub>O<sub>4</sub> demonstrates the superimposition of the diffraction peaks with the pure magnetite without a change in the crystal phase. It is worth noting that after incorporating the Pd on the magnetite, the structural lattice arrangement of the parent magnetite remains preserved, leading to the conclusion that the added Pd anchored on the surface of the magnetite instead of the lattice unit cell, as it did not dilate the peaks or alter the structure of the parent magnetite. The crystallite size evaluated from the Debye–Scherrer equation was estimated to be less than 10 nm, further confirmed by TEM. XRD detects the presence of Pd with the appearance of the small diffraction peaks at 2θ = 40.10 and 46.62° (card no.: 01–076–7157) (Figure S5b). This could be attributed to metallic Pd(111) being dispersed over the spherical solid surface of the magnetite.

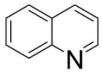
To obtain further information about the elemental composition and the electronic structure of the constituent elements, X-ray photoelectron spectroscopy (XPS) was employed, and the results are presented in Figure 1k,l. The results of the typical survey confirm the presence of Fe and Pd, as depicted in Figure 1k. The oxidation states were investigated by fitting the emission curve of Pd using the Gaussian method, and the results of the spin–orbit coupling constant Δ = 5.3 eV led to the further identification of the Pd species (Figure 1l). The peaks at 335.8 eV (3d<sub>5/2</sub>) and 340.9 eV (3d<sub>3/2</sub>) are attributed to the Pd<sup>0</sup> species, which indicates that potassium tetrachloropalladate (K<sub>2</sub>PdCl<sub>4</sub>) has been effectively reduced to metallic Pd onto the magnetite matrix during the reduction process using aqueous ammonia as a reducing agent.<sup>39</sup> However, the binding energies at 337.6 and 342.9 eV assigned to the Pd(II) species may result from the partial oxidation of the Pd nanoparticles for a long period of exposure to ambient conditions.

The magnetic properties of the Fe<sub>3</sub>O<sub>4</sub> and Pd@Fe<sub>3</sub>O<sub>4</sub> were measured by a superconducting quantum interference device (SQUID) at 300 K, and the results are shown in Figure 2. The

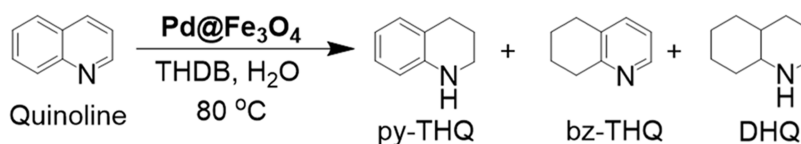


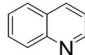
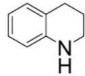
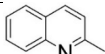
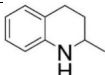
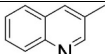
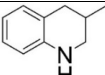
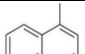
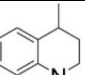
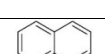
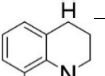
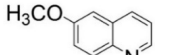
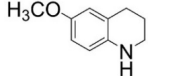
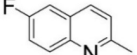
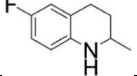
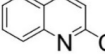
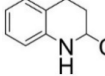
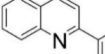
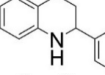
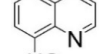
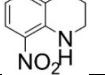
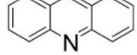
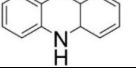
**Figure 2.** Magnetic susceptibility of Fe<sub>3</sub>O<sub>4</sub> and Pd@Fe<sub>3</sub>O<sub>4</sub> and with the coercivity data of Pd@Fe<sub>3</sub>O<sub>4</sub> (inset).

Table 1. Optimization of Catalytic Transfer Hydrogenation Reaction Using Pd@Fe<sub>3</sub>O<sub>4</sub> in Water as a Solvent<sup>a</sup>

Entry	Substrate	Temp (°C)	THDB (mmol)	Time (min)	Conv. <sup>b</sup> (%)	Select. <sup>c</sup> (%)
1		50	2	60	95	>99
2		60	2	60	96	>99
3		80	2	60	>99	>99
4		80	1	60	87	>99
5		80	2	60	>99	>99
6		80	3	60	>99	>99
7		80	2	10	>95	>99
8		80	2	30	>97	>99
9		80	2	60	>99	>99
10 <sup>d</sup>		80	2	60	27	>99

<sup>a</sup>5 mg catalyst, 0.5 mmol of quinoline in 10 mL of H<sub>2</sub>O. <sup>b</sup>The products measured by GC. <sup>c</sup>Identified by GC-MS. <sup>d</sup>Blank reaction.

Table 2. Pd@Fe<sub>3</sub>O<sub>4</sub>-Catalyzed Transfer Hydrogenation of Quinoline Derivatives in Water as a Solvent<sup>a</sup>

Entry	Substrate	Product	Conv. <sup>b</sup> (%)	Select. <sup>c</sup> (%)
1			>99%	>99%
2			57%	>99%
3			92%	>99%
4			67%	>99%
5			44%	>99%
6			>99%	>99%
7			76%	>99%
8			10	<2
9			6	>99%
10 <sup>d</sup>			54%	47%
11			45%	>99%

<sup>a</sup>5 mg catalyst, 0.5 mmol of quinoline in 10 mL H<sub>2</sub>O, 2 mmol THDB for 60 min at 80 °C. <sup>b</sup>The products measured by GC. <sup>c</sup>Identified by GC-MS. <sup>d</sup>3 mmol THDB at 50 °C for 420 min.

hysteresis loops of Fe<sub>3</sub>O<sub>4</sub> indicate that the saturation magnetization ( $M_s$ ) is 60.9 emu/g with a coercivity ( $H_c$ ) of 6.2 Oe. However, the decoration of Pd nanoparticles on the

surface of Fe<sub>3</sub>O<sub>4</sub> affected its magnetic nature, yielding 51.9 emu/g. The slight decrease of the  $M_s$  value of Pd@Fe<sub>3</sub>O<sub>4</sub> can be due to the addition of the nonmagnetic element (Pd), but it

Table 3. Pd@Fe<sub>3</sub>O<sub>4</sub>-Catalyzed Transfer Hydrogenation of Nitroarene in Water<sup>a</sup>

4-Nitrophenol  $\xrightarrow[\text{THDB, H}_2\text{O}]{\text{Pd@Fe}_3\text{O}_4, 80\text{ }^\circ\text{C}}$  4-Aminophenol

Entry	Substrate	Product	Temp. (°C)	Conv. <sup>b</sup> (%)	Select. <sup>c</sup> (%)
1			50	<5	Nd
2			80	>99	>99
3			80	>99	>99
4			80	>99	>99
5			80	>99	>99
6			80	>99	>99
7			80	87	>99
8			80	>99	<2
9 <sup>d</sup>			50	>99	70
10 <sup>d</sup>			50	42	<2

<sup>a</sup>5 mg catalyst, 0.5 mmol of nitroarene in 10 mL of H<sub>2</sub>O, 2 mmol of THDB at 80 °C for 60 min. <sup>b</sup>Measured by GC. <sup>c</sup>Identified by GC-MS. <sup>d</sup>Duration of 1440 min; nd: not determined.

is still magnetic enough to separate these catalysts after the reaction by using a magnet. Furthermore, a lower magnetic coercivity value (6.1 Oe) is recorded, indicating a single magnetic domain with supermagnetic nature.

**Catalysis.** *Catalytic Transfer Hydrogen of Quinoline.* Quinoline was used as a benchmark substrate for the catalytic transfer hydrogenation reaction in water using Pd@Fe<sub>3</sub>O<sub>4</sub> as a catalyst (Tables 1 and 2). Instead of compressed hydrogen gas in cylinders, the transfer hydrogenation activity was evaluated by using water and tetrahydroxydiboron (THDB) as a sacrificial agent. The THDB requirement was investigated in the presence of the catalyst, and no conversion was noted. In the absence of the Pd@Fe<sub>3</sub>O<sub>4</sub> catalyst, the reaction proceeded at a much slower rate in the presence of THDB, resulting in <30% conversion in 24 h. The progress of the reaction was monitored by TLC and GC, and the products were identified by GC-MS. Suitable reaction conditions were developed by optimizing several parameters, such as temperature, amount of THDB, and duration of the reaction. Initially, the transfer hydrogenation reaction was carried out at 50 °C with the 2 equiv of THDB, resulting in a 95% quinoline hydrogenated product with >99% chemoselectivity toward py-THQ in 60 min (Table 1, entry 1). However, complete conversion of

quinoline was achieved as the temperature increased from 60 to 80 °C with unaffected selectivity under the same duration (entries 2–3). Then, the amount of THDB was optimized (entries 4–6). With the use of 1 equiv of THDB, 87% quinoline was converted to >99% pyridine-ring hydrogenated product (entry 4). The optimum conversion was achieved with the 2 equiv of THDB in 60 min, and after further increasing the amount, no deteriorating effect on the activity or selectivity was observed. Also, the duration of the reaction was established by withdrawing the sample from the reaction in the time intervals of 10, 30, and 60 min, and the samples were injected into GC-MS (entries 7–9). Results demonstrated that the time needed to complete the conversion of quinoline to its corresponding hydrogenated product was 60 min. Therefore, 0.5 mmol of quinoline can be completely hydrogenated in 60 min using 2 equiv THDB at 80 °C in water as a solvent.

The scope of the transfer hydrogenation process was then investigated using the Pd@Fe<sub>3</sub>O<sub>4</sub> catalyst under the optimized reaction conditions, and results are summarized in Table 2. In this context, various electron-donating and -withdrawing groups attached to quinoline derivatives were tested, and their functional group tolerance toward the transfer hydrogenation reactions was evaluated. For instance, 57% of the 2-

methyl quinoline was converted to a pyridine-ring hydrogenated product with >99% selectivity (entry 2) in 60 min. Delightfully, the enhanced conversion (>92%) was achieved from a 3-methylquinoline hydrogenation reaction under the same reaction condition (entry 3). The enhanced conversion could be due to the lower steric influence of the methyl group at the pyridyl nitrogen, which is responsible for the effective interaction with the catalytic metal center. However, the reactivity of 4-methylquinoline drops (67%, entry 4) significantly while the selectivity remained unchanged. As expected, the conversion (44%) dropped significantly when the methyl group was attached to the carbocyclic ring to the C8 position of 8-methylquinoline (entry 5). Therefore, the hydrogenation reactivity trend with Pd@Fe<sub>3</sub>O<sub>4</sub> catalyst was established as 3-Me > 4-Me > 2-Me > 8-Me quinoline.

6-Methoxyquinoline was quantitatively hydrogenated to produce >99% pyridine-ring hydrogenated product (entry 6). However, replacing the electron-donating -OCH<sub>3</sub> group with the highly electron-withdrawing F atom at the same position of the carbocyclic ring negatively impacted the conversion negatively (entry 7). Surprisingly, when 2-chloroquinoline was subjected to the same hydrogenation condition, only 10% conversion was achieved (entry 8). This is probably the inability to disrupt the strong hydrogen bonding with the incoming hydrogen to form the N...H...Cl bridge, which hinders the metal from coming closer to the pyridine ring hydrogenation.<sup>40</sup> Moreover, the 2-chloroquinoline hydrogenation produces only dechlorinated quinoline instead of any hydrogenation product. Also, due to the steric effect, 2-phenylquinoline, which is a challenging substrate due to the bulkier -Ph group attached to the adjacent carbon to the nitrogen atom of the pyridine ring, resulted in drastically lower conversion (entry 9). 8-Nitroquinoline, containing two competitive functional groups (pyridine ring and nitro group), was employed for the hydrogenation reaction (entry 10). The results show a 54% conversion rate and a 47% chemoselectivity for py-THQ. Acridine responded smoothly, affording the desired product in 45% conversion with >99% pyridine ring hydrogenation selectivity (entry 11). This hydrogenated product obtained from acridine is often used as an important building block for producing several anticancer drugs.

**Hydrogenation of Nitroarene Compounds.** The transfer hydrogenation of the nitroarenes compounds using Pd@Fe<sub>3</sub>O<sub>4</sub> is evaluated, and the results are shown in Table 3. The reduction of nitroarenes to corresponding amines is a frequently used process in the industry.<sup>41</sup> For instance, anilines, which are important precursors for rubber chemicals, pesticides, dyes, and pharmaceuticals, are obtained from the nitroarenes hydrogenation reactions.<sup>30,42,43</sup> However, the challenge with the reduction process is achieving high product selectivity in the presence of multiple competitive functional groups with high reaction rates.<sup>44</sup> In addition, the prospect of multiple intermediate product formations, such as azobenzene, azoxybenzene, or hydroxylamines, during the hydrogenation process cannot be ruled out.<sup>45</sup> This is because the reduction proceeds stepwise, as Haber proposed in 1898, and the subsequent reactions between the intermediates may lead to the formation of multiple coupling products.<sup>45,46</sup> Therefore, the discovery of catalytic systems with exclusive aniline selectivity and a high functional group tolerance is highly desirable. In this context, the quinoline hydrogenation activity and selectivity encourage us to further investigate the Pd@

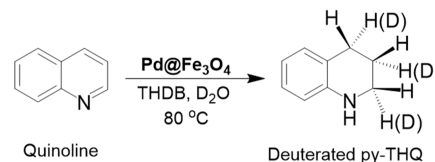
Fe<sub>3</sub>O<sub>4</sub> activity and selectivity for the nitroarenes reduction in water.

4-Nitrophenol was chosen as a benchmark substrate for the catalytic reduction using Pd@Fe<sub>3</sub>O<sub>4</sub> catalysts, and the results are shown in Table 3. Initially, the reaction was carried out at 50 °C using 2 equiv of THDB in water, and no reduced product was detected (Table 3, entry 1). Then, the superior activity of the catalyst is noted when the temperature is increased to 80 °C, which results in a quantitative conversion of 4-nitrophenol to 4-aminophenol with >99% amine selectivity in 1 h (entry 2). However, in the early stages of the reaction (after 10 min), azobenzene was the main product. As the reaction proceeded, the selectivity of azobenzene dropped gradually, and 4-aminophenol emerged as a main product in 1 h. Hence, the reaction sequence and the intermediate formation detected during the reaction indicate that the nitroarene hydrogenation reaction is proceeding by following the Haber mechanism.<sup>47</sup> Nitrobenzene is quantitatively converted to aniline (entry 3).

Next, the effect of the position of the electron-donating group in the nitrobenzene moieties was evaluated (entries 4–6). When 2,6-dimethylnitrobenzene was employed, the conversion dropped to 87% with >99% amine selectivity (entry 7). This decreased conversion may be due to the steric hindrance operating around the -NO<sub>2</sub> functional group by the two adjacent -Me groups obstructing access to the metal center for effective interaction. The hydrogenation of 4-chloro nitrobenzene under the same reaction conditions yielded quantitative conversion with a complete dichlorination product at 80 °C in 1 h (entry 8). However, a significant improvement in selectivity (70%) was observed by slowing the reaction rate through lowering the reaction temperature to 50 °C and prolonging the reaction time to 10 h (entry 9). A complete debromination occurs for the 4-bromo-nitrobenzene reaction even at 50 °C.

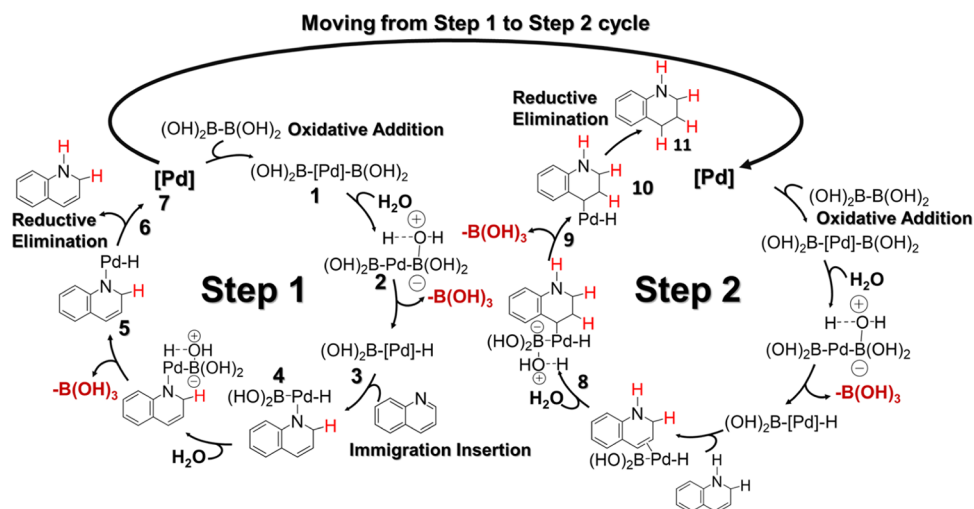
**Isotope Labeling Studies.** Investigations were conducted to understand the origin of hydrogen in the Pd@Fe<sub>3</sub>O<sub>4</sub>-catalyzed transfer hydrogenation reaction. A deuterium-labeling experiment was conducted using quinoline (Scheme 2) as the

### Scheme 2. Isotope Labeling Experiment

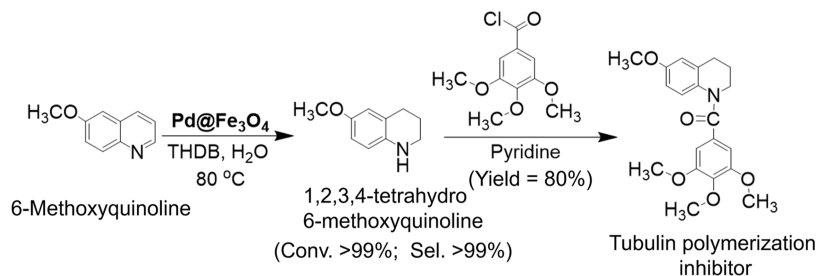


standard substrate by replacing H<sub>2</sub>O with D<sub>2</sub>O as a solvent in the presence of THDB at 80 °C. A deuterated py-THQ was detected by NMR and GC-MS (Supporting Information), showing that the C2, C3, and C4 positions were deuterated. However, deuteration of the nitrogen atom was not detected as anticipated. Probably, it is due to the rapid exchange of deuterium atoms with hydrogen atoms derived from a trace of water during the synthesis process.<sup>48,49</sup> The results showed how important water molecules are in the hydrogenation process. It is also possible to conclude that water is the source of hydrogen in the reaction, and the boron-based Lewis acid, THDB, plays an active role in activating the water molecule to generate hydrogen through a complex reaction mechanism, which will be discussed in a subsequent section.

**Scheme 3. Illustration of a Possible Mechanism of Pd@Fe<sub>3</sub>O<sub>4</sub> Catalyst for Quinoline Hydrogenation Reaction in H<sub>2</sub>O Using THDB**



**Scheme 4. Synthesis of Tubular Polymerization Inhibitor Using Pd@Fe<sub>3</sub>O<sub>4</sub> Catalyst**



We propose the following putative catalytic cycles based on our observations from isotopic labeling studies for the quinoline transfer hydrogenation reaction (Scheme 3). First, in step 1, the B–B bond from the THDB undergoes oxidative addition to metallic palladium to form  $Pd^{2+}$  species 1. Then, the lone pairs of oxygen atoms are activated in the presence of an electron-deficient boron atom to afford compound 2. Boric acid is eliminated to produce Pd-hydride complex 3 ( $-H_3BO_3$ ). In this context, quinoline is introduced into the catalytic cycles. The Pd-hydride boron complex attempts to coordinate with the N site, owing to its elevated electronegativity. This coordination leads to the formation of  $-N-Pd-B(OH)_2$  adduct 4. Subsequently, water coordinates with the second boron atom, resulting in compound 5. This coordination event facilitates the transfer of hydrogen, leading to the formation of the second palladium hydride intermediate 6. Ultimately, reductive elimination occurs, resulting in the production of partially hydrogenated product 7. In step 2, the same catalytic cycles as in step 1 are expected to continue to hydrogenate the remaining double bond existing in the quinoline molecule to afford the fully N-containing ring hydrogenated product of quinoline.

**Application. Application of Quinoline Hydrogenation: Synthesis of Tubular Polymerization Inhibitor.** Antimitotic agents, such as taxanes and vinca alkaloids, are important chemotherapy drugs in oncology.<sup>4</sup> However, excessive surrounding system toxicity, cumbersome preparation techniques, and drug resistance lead to a search for an effective alternative to antimitotic drugs. Recently, it has been found that tubulins can act as a disrupting agent by blocking the

blood supply to the endothelial cells of tumor vessels, slowing down cancer cell proliferation.<sup>34,50</sup> Therefore, the encouraging antitumor proliferation activity has stimulated interest in the design and synthesis of a variety of derivatives or analogs.<sup>51</sup> Some of these biologically active molecules are based on 1,2,3,4-THQ scaffolds. Despite the availability of numerous synthetic routes for this heterocyclic skeleton, partial hydrogenation of N-heteroaromatics is a straightforward and practical method to produce N-ring hydrogenated heterocycles. Therefore, a synthetic protocol developed in this study can be extended to synthesize the tubulin polymerization inhibitor. In this context, 6-methoxyquinoline is hydrogenated using  $Pd@Fe_3O_4$  to produce 6-methoxy-1,2,3,4-tetrahydroquinoline with >99% chemoselectivity (Scheme 4). Thereafter, the N atom of the hydrogenated ring of 6-methoxy-1,2,3,4-tetrahydroquinoline is coupled with the commercially available 3,4,5-trimethoxybenzoyl chloride in pyridine solvent to produce the N-amidated tubulin polymerization inhibitor (6-methoxy-3,4-dihydroquinolin-1(2H)-yl) (3,4,5-trimethoxyphenyl)methanone with an 80% yield. A detailed procedure is as follows: In a Schlenk tube, 6-methoxyquinoline-1,2,3,4-tetrahydroquinoline (1.3 mmol, 212 mg) was taken in anhydrous pyridine (5 mL), and then 1.5 equiv of 3,4,5-trimethoxybenzoyl chloride (1.95 mmol, 450 mg) were added. The mixture continued to stir at room temperature under an inert atmosphere for 24 h, and the crude product was extracted with dichloromethane. The combined organic layers were washed with a 5% aqueous HCl solution, dried using  $Na_2SO_4$ , and then purified by column chromatography using hexane



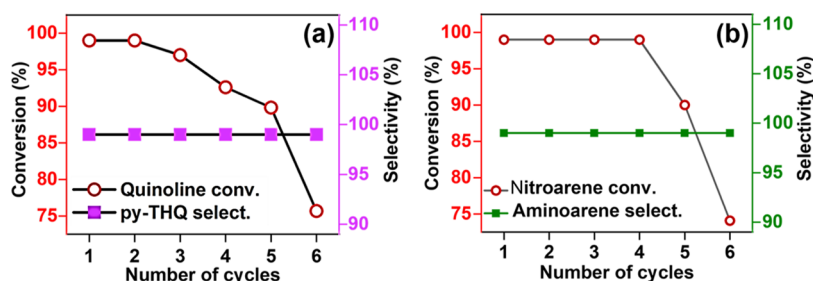


**Figure 3.** Reusability of the catalyst for the transfer hydrogenation reaction under the optimized conditions for (a) quinoline and (b) nitrobenzene.

and ethyl acetate (7:3) as an eluent to produce N-amidated product of 380 mg (80% yield).

**Reusability.** The reusability of the catalyst is an important requirement for its sustainable development in terms of economic and environmental concerns. In this study, the catalyst was recovered after the hydrogenation by using a simple external magnet, washed several times using deionized water, and then reused without the addition of any fresh catalyst for the next cycles of the transfer hydrogenation reaction in water. The results showed that the conversion of quinoline remained unchanged until the second consecutive cycle, and then a gradual decrease in conversion was observed, as shown in Figure 3a. After the sixth cycle, 74% conversion was noted with unaffected chemoselectivity. The probable reason for the loss of activity was investigated using Brunauer–Emmett–Teller (BET) and FTIR studies (Figure S3). BET shows a decrease in surface area from 108.1 to 94.3 m<sup>2</sup>/g after the use of six consecutive cycles. This is probably due to the strong attachment of the quinoline and its corresponding hydrogenated product (py-THQ) blocking the pores, which results in the poisoning of the catalyst. This hypothesis is supported by the FTIR studies, which show the presence of C=N and C–N stretching vibrations. Additionally, the loss of catalyst during the recycling procedure could also contribute to the lower conversion. The stability of the catalyst for nitrobenzene hydrogenation was also evaluated, and improved stability of the catalyst for a higher number of cycles was observed. It was found that catalyst Pd@Fe<sub>3</sub>O<sub>4</sub> retained its original activity up to the fourth consecutive cycle with quantitative selectivity (Figure 3b).

## CONCLUSIONS

In this study, a facile Pd@Fe<sub>3</sub>O<sub>4</sub> nanocatalyst fabrication strategy that provides an efficient and magnetically separable catalyst was demonstrated. Ultrafine Pd nanoparticles were placed on the surface of superparamagnetic iron oxide nanoparticles (SPIONs) for the transfer hydrogenation of N-heteroarene and nitroaromatic compounds under mild reaction conditions in water. THDB was used to perform chemoselective hydrogenation of quinoline, yielding >99% conversion with optimum selectivity toward the pyridine ring hydrogenated product. Nitroarenes were quantitatively hydrogenated in water to produce corresponding aromatic amines. Isotopic labeling studies were performed to investigate the mechanism of transfer hydrogenation, as well as the role of solvent and THDB. A possible reaction mechanism was proposed. The hydrogenation protocol was extended to synthesize a biologically active tubulin polymerization inhibitor, a chemotherapeutic drug for cancer. The developed catalyst has demonstrated higher reusability for the nitroarene hydrogenation reaction. The use of the developed strategy that

does not require hydrogen pressure, has higher activity and selectivity, uses a green solvent, ligand-free, easy to separate, and is environmentally benign holds great promise for industrial applications. Other catalytic transformation reactions are currently under investigation in our laboratory.

## ASSOCIATED CONTENT

### Supporting Information

The Supporting Information is available free of charge at <https://pubs.acs.org/doi/10.1021/acsomega.3c07550>.

FTIR spectra of Pure Fe<sub>3</sub>O<sub>4</sub> and Pd@Fe<sub>3</sub>O<sub>4</sub> (Figure S1); Raman spectra of pure Fe<sub>3</sub>O<sub>4</sub> and Pd@Fe<sub>3</sub>O<sub>4</sub> catalyst (Figure S2); ICP-OES data for 7%Pd@Fe<sub>3</sub>O<sub>4</sub> and 15%Pd@Fe<sub>3</sub>O<sub>4</sub> catalysts (Table S1); size distribution curve of Pd@Fe<sub>3</sub>O<sub>4</sub> based on TEM analysis (Figure S3); ζ-potential for Pd@Fe<sub>3</sub>O<sub>4</sub> in water (Figure S4); XRD references for Pd@Fe<sub>3</sub>O<sub>4</sub> with insertion of card info: 01–076–7157 related to (a) magnetite, and card info: 00–005–0681 related to (b) Pd<sup>0</sup> (Figure S5); quinoline hydrogenation after 60 min, GC and identification of product by GC-MS of the peak R<sub>t</sub> = 15.82 (Figure S6); hydrogenation of 6-methoxyquinoline, GC and identification of product by GC-MS of the peak R<sub>t</sub> = 27.37 (Figure S7); 2-chloro-quinoline spectra by gas chromatography–mass, GC and identification of product by GC-MS of the peaks R<sub>t</sub> = 5.851, and GC-MS of the peak R<sub>t</sub> = 18.96 (Figure S8); 6-chloro-quinoline spectra by gas chromatography–mass, GC, identification of product by GC-MS of the peak at R<sub>t</sub> = 13.182, GC-MS of the peak at R<sub>t</sub> = 15.842, and GC-MS of the peak at R<sub>t</sub> = 18.23 (Figure S9); nitroarene hydrogenation to produce aminobenzene after 60 min, GC and identification of product by GC-MS of the peak at R<sub>t</sub> = 6.11 (Figure S10); 1-chloro-4-nitrobenzene spectra by gas chromatography–mass, GC and identification of product by GC-MS of the peak at R<sub>t</sub> = 6.015, GC-MS of the peak at R<sub>t</sub> = 12.332, and GC-MS of the peak at R<sub>t</sub> = 13.343 (Figure S11); 1-bromo-4-nitrobenzene spectra by gas chromatography–mass, GC and identification of product by GC-MS of the peak R<sub>t</sub> = 6.00, GC-MS of the peak at R<sub>t</sub> = 8.985, GC-MS of the peak R<sub>t</sub> = 15.875 (Figure S12); H-insertion in quinoline spectra using H<sub>2</sub>O, GC and identification of product by GC-MS of the peak R<sub>t</sub> = 15.82 (Figure S13); D-insertion in quinoline spectra for isotope reaction using D<sub>2</sub>O, GC and identification of product by GC-MS of the peak R<sub>t</sub> = 15.78 (Figure S14); tubulin polymerization inhibitor characterization result by GC-MS, GC and identification of product by GC-MS of the peak R<sub>t</sub> = 48.773 (Figure S15); <sup>1</sup>H NMR spectra for H-insertion on quinoline

compound (Figure S16);  $^{13}\text{C}$  NMR spectra for H-insertion on quinoline compound (Figure S17);  $^1\text{H}$  NMR spectra for D-insertion on quinoline compound (Figure S18);  $^{13}\text{C}$  NMR spectra for D-insertion on quinoline compound (Figure S19);  $^1\text{H}$  NMR spectra for tubulin polymerization inhibitor (Figure S20);  $^{13}\text{C}$  NMR spectra for tubulin polymerization inhibitor (Figure S21); previously reported catalysts for hydrogenation of quinoline and nitroarene by transfer hydrogenation reaction in water (Table S2); FTIR and BET of the spent  $\text{Pd}@\text{Fe}_3\text{O}_4$  catalyst (Figure S22); and XPS spectra for Fe (Figure S23) (PDF)

## AUTHOR INFORMATION

### Corresponding Author

**M. Nasiruzzaman Shaikh** – Interdisciplinary Research Center for Hydrogen and Energy Storage (IRC-HES), King Fahd University of Petroleum and Minerals (KFUPM), Dhahran 31261, Saudi Arabia; [orcid.org/0000-0002-9549-6322](https://orcid.org/0000-0002-9549-6322); Email: [mshaikh@kfupm.edu.sa](mailto:mshaikh@kfupm.edu.sa)

### Authors

**Huda S. Alghamdi** – Interdisciplinary Research Center for Hydrogen and Energy Storage (IRC-HES), King Fahd University of Petroleum and Minerals (KFUPM), Dhahran 31261, Saudi Arabia

**Afnan M. Ajeebi** – Interdisciplinary Research Center for Hydrogen and Energy Storage (IRC-HES), King Fahd University of Petroleum and Minerals (KFUPM), Dhahran 31261, Saudi Arabia

**Md. Abdul Aziz** – Interdisciplinary Research Center for Hydrogen and Energy Storage (IRC-HES), King Fahd University of Petroleum and Minerals (KFUPM), Dhahran 31261, Saudi Arabia; [orcid.org/0000-0002-1537-2785](https://orcid.org/0000-0002-1537-2785)

**Atif Saeed Alzahrani** – Material Science Engineering Department, King Fahd University of Petroleum and Minerals (KFUPM), Dhahran 31261, Saudi Arabia

Complete contact information is available at:

<https://pubs.acs.org/10.1021/acsomega.3c07550>

### Notes

The authors declare no competing financial interest.

## ACKNOWLEDGMENTS

The authors gratefully acknowledge the support of the Interdisciplinary Research Center for Hydrogen and Energy Storage (IRC-HES), King Fahd University of Petroleum & Minerals (KFUPM), for funding this work through grant number INHE2212.

## REFERENCES

- (1) *Catalysis of Organic Reactions*, Sowa, Jr., Ed.; CRC Press, 2005.
- (2) Bálint, J.; Egri, G.; Fogassy, E.; Böcskei, Z.; Simon, K.; Gajáry, A.; Friesz, A. Synthesis, Absolute Configuration and Intermediates of 9-Fluoro-6, 7-Dihydro-5-Methyl-1-Oxo-1H, 5H-Benzo [i, j] Quinolizine-2-Carboxylic Acid (Flumequine). *Tetrahedron: Asymmetry* **1999**, *10*, 1079–1087.
- (3) Guinó, M.; Phua, P. H.; Caille, J.-C.; Hii, K. K. A Concise Asymmetric Synthesis of Torcetrapib. *J. Org. Chem.* **2007**, *72*, 6290–6293.
- (4) Liou, J.-P.; Wu, Z.-Y.; Kuo, C.-C.; Chang, C.-Y.; Lu, P.-Y.; Chen, C.-M.; Hsieh, H.-P.; Chang, J.-Y. Discovery of 4-Amino and 4-Hydroxy-1-Aroylindoles as Potent Tubulin Polymerization Inhibitors. *J. Med. Chem.* **2008**, *51*, 4351–4355.
- (5) Chaudhaery, S. S.; Roy, K. K.; Shakya, N.; Saxena, G.; Sammi, S. R.; Nazir, A.; Nath, C.; Saxena, A. K. Novel Carbamates as Orally Active Acetylcholinesterase Inhibitors Found to Improve Scopolamine-Induced Cognition Impairment: Pharmacophore-Based Virtual Screening, Synthesis, and Pharmacology. *J. Med. Chem.* **2010**, *53*, 6490–6505.
- (6) Voigt, W.; Mannhold, R.; Limberg, J.; Blaschke, G. Interactions of Antiarrhythmics with Artificial Phospholipid Membranes. *J. Pharm. Sci.* **1988**, *77*, 1018–1020.
- (7) Yang, C. H.; Chen, X.; Li, H.; Wei, W.; Yang, Z.; Chang, J. Iodine Catalyzed Reduction of Quinolines under Mild Reaction Conditions. *Chem. Commun.* **2018**, *54*, 8622–8625.
- (8) Shaikh, M. N.; Aziz, M. A.; Kalanthoden, A. N.; Helal, A.; Hakeem, A. S.; Bououdina, M. Facile Hydrogenation of N-Heteroarenes by Magnetic Nanoparticle-Supported Sub-Nanometric Rh Catalysts in Aqueous Medium. *Catal. Sci. Technol.* **2018**, *8*, 4709–4717.
- (9) Sandl, S.; Maier, T. M.; van Leest, N. P.; Kröncke, S.; Chakraborty, U.; Demeshko, S.; Koszinowski, K.; de Bruin, B.; Meyer, F.; Bodensteiner, M.; Herrmann, C.; Wolf, R.; von Wangelin, A. J. Cobalt-Catalyzed Hydrogenations via Olefin Cobaltate and Hydride Intermediates. *ACS Catal.* **2019**, *9*, 7596–7606.
- (10) Papa, V.; Cao, Y.; Spannenberg, A.; Junge, K.; Beller, M. Development of a Practical Non-Noble Metal Catalyst for Hydrogenation of N-Heteroarenes. *Nat. Catal.* **2020**, *3*, 135–142.
- (11) Adam, R.; Cabrero-Antonino, J. R.; Spannenberg, A.; Junge, K.; Jackstell, R.; Beller, M. A General and Highly Selective Cobalt-Catalyzed Hydrogenation of N-Heteroarenes under Mild Reaction Conditions. *Angew. Chem.* **2017**, *129*, 3264–3268.
- (12) Pang, M.; Chen, J.-Y.; Zhang, S.; Liao, R.-Z.; Tung, C.-H.; Wang, W. Controlled Partial Transfer Hydrogenation of Quinolines by Cobalt-Amido Cooperative Catalysis. *Nat. Commun.* **2020**, *11*, No. 1249.
- (13) Genet, J.-P.; Ayad, T.; Ratovelomanana-Vidal, V. Electron-Deficient Diphosphines: The Impact of DIFLUORPHOS in Asymmetric Catalysis. *Chem. Rev.* **2014**, *114*, 2824–2880.
- (14) Wu, J.; Barnard, J. H.; Zhang, Y.; Talwar, D.; Robertson, C. M.; Xiao, J. Robust Cyclometallated Ir (III) Catalysts for the Homogeneous Hydrogenation of N-Heterocycles under Mild Conditions. *Chem. Commun.* **2013**, *49*, 7052–7054.
- (15) Tole, T. T.; Jordaan, J. H. L.; Vosloo, H.  $\alpha$ -Pyridinyl Alcohols,  $\alpha$ ,  $\alpha'$ -Pyridine Diols,  $\alpha$ -Bipyridinyl Alcohols, and  $\alpha$ ,  $\alpha'$ -Bipyridine Diols as Structure Motifs Towards Important Organic Molecules and Transition Metal Complexes. *Curr. Org. Synth.* **2020**, *17*, 344–366.
- (16) Tang, F.; Zhang, G.; Wang, L.; Huang, J.; Liu, Y.-N. Unsymmetrically N, S-Coordinated Single-Atom Cobalt with Electron Redistribution for Catalytic Hydrogenation of Quinolines. *J. Catal.* **2022**, *414*, 101–108.
- (17) Shaikh, M. N.; Aziz, M. A.; Helal, A.; Bououdina, M.; Yamani, Z. H.; Kim, T.-J. Magnetic Nanoparticle-Supported Ferrocenylphosphine: A Reusable Catalyst for Hydroformylation of Alkene and Mizoroki–Heck Olefination. *RSC Adv.* **2016**, *6*, 41687–41695.
- (18) Wei, Z.; Shao, F.; Wang, J. Recent Advances in Heterogeneous Catalytic Hydrogenation and Dehydrogenation of N-Heterocycles. *Chin. J. Catal.* **2019**, *40*, 980–1002.
- (19) Wei, Z.; Chen, Y.; Wang, J.; Su, D.; Tang, M.; Mao, S.; Wang, Y. Cobalt Encapsulated in N-Doped Graphene Layers: An Efficient and Stable Catalyst for Hydrogenation of Quinoline Compounds. *ACS Catal.* **2016**, *6*, 5816–5822.
- (20) Karakulina, A.; Gopakumar, A.; Akçok, İ.; Roulier, B. L.; LaGrange, T.; Katsyuba, S. A.; Das, S.; Dyson, P. J. A Rhodium Nanoparticle–Lewis Acidic Ionic Liquid Catalyst for the Chemo-selective Reduction of Heteroarenes. *Angew. Chem.* **2016**, *128*, 300–304.
- (21) Wei, X.; Zhou, M.; Zhang, X.; Wang, X.; Wu, Z. Amphiphilic Mesoporous Sandwich-Structured Catalysts for Selective Hydro-

genation of 4-Nitrostyrene in Water. *ACS Appl. Mater. Interfaces* **2019**, *11*, 39116–39124.

(22) Nie, R.; Tao, Y.; Nie, Y.; Lu, T.; Wang, J.; Zhang, Y.; Lu, X.; Xu, C. C. Recent Advances in Catalytic Transfer Hydrogenation with Formic Acid over Heterogeneous Transition Metal Catalysts. *ACS Catal.* **2021**, *11*, 1071–1095.

(23) Gelis, C.; Heusler, A.; Nairoukh, Z.; Glorius, F. Catalytic Transfer Hydrogenation of Arenes and Heteroarenes. *Chem. - Eur. J.* **2020**, *26*, 14090–14094.

(24) Cui, X.; Huang, W.; Wu, L. Zirconium-Hydride-Catalyzed Transfer Hydrogenation of Quinolines and Indoles with Ammonia Borane. *Org. Chem. Front.* **2021**, *8*, S002–S007.

(25) El kadiri, M.; El Assimi, T.; Thébault, P.; El Meziane, A.; Royer, S.; El Kadib, A.; Gouhier, G.; Lahcini, M. Bismuth Nanoparticles Supported on Biobased Chitosan as Sustainable Catalysts for the Selective Hydrogenation of Nitroarenes. *ACS Appl. Nano Mater.* **2023**, *6* (6), 4017–4027.

(26) Zhou, P.; Li, D.; Jin, S.; Chen, S.; Zhang, Z. Catalytic Transfer Hydrogenation of Nitro Compounds into Amines over Magnetic Graphene Oxide Supported Pd Nanoparticles. *Int. J. Hydrogen Energy* **2016**, *41* (34), 15218–15224.

(27) Simamora, P.; Manullang, M.; Munthe, J.; Rajaguguk, J. The Structural and Morphology Properties of Fe<sub>3</sub>O<sub>4</sub>/Ppy Nanocomposite. *J. Phys.: Conf. Ser.* **2018**, *1120*, No. 012063.

(28) Xuan, S.; Wang, F.; Lai, J. M. Y.; Sham, K. W. Y.; Wang, Y.-X. J.; Lee, S.-F.; Yu, J. C.; Cheng, C. H. K.; Leung, K. C.-F. Synthesis of Biocompatible, Mesoporous Fe<sub>3</sub>O<sub>4</sub> Nano/Microspheres with Large Surface Area for Magnetic Resonance Imaging and Therapeutic Applications. *ACS Appl. Mater. Interfaces* **2011**, *3*, 237–244.

(29) Shaikh, M. N.; Bououdina, M.; Jimoh, A. A.; Aziz, M. A.; Helal, A.; Hakeem, A. S.; Yamani, Z. H.; Kim, T.-J. The Rhodium Complex of Bis(Diphenylphosphinomethyl)Dopamine-Coated Magnetic Nanoparticles as an Efficient and Reusable Catalyst for Hydroformylation of Olefins. *New J. Chem.* **2015**, *39*, 7293–7299.

(30) Shaikh, M. N.; Aziz, A.; Hussain, S. M. S.; Helal, A. Rh-Complex Supported on Magnetic Nanoparticles as Catalysts for Hydroformylations and Transfer Hydrogenation Reactions. *Asian J. Org. Chem.* **2022**, *11*, No. e202100759.

(31) Chaki, S. H.; Malek, T. J.; Chaudhary, M. D.; Tailor, J. P.; Deshpande, M. P. Magnetic Fe<sub>3</sub>O<sub>4</sub> Nanoparticles Synthesis by Wet Chemical Reduction and Their Characterization. *Adv. Nat. Sci.: Nanosci. Nanotechnol.* **2015**, *6*, No. 035009.

(32) Niu, H.; Lu, J.; Song, J.; Pan, L.; Zhang, X.; Wang, L.; Zou, J. J. Iron Oxide as a Catalyst for Nitroarene Hydrogenation: Important Role of Oxygen Vacancies. *Ind. Eng. Chem. Res.* **2016**, *55*, 8527–8533.

(33) Qu, X. F.; Yao, Q. Z.; Zhou, G. T.; Fu, S. Q.; Huang, J. L. Formation of Hollow Magnetite Microspheres and Their Evolution into Durian-like Architectures. *J. Phys. Chem. C* **2010**, *114*, 8734–8740.

(34) Zhang, Y.; Grass, M. E.; Habas, S. E.; Tao, F.; Zhang, T.; Yang, P.; Somorjai, G. A. One-Step Polyol Synthesis and Langmuir–Blodgett Monolayer Formation of Size-Tunable Monodisperse Rhodium Nanocrystals with Catalytically Active (111) Surface Structures. *J. Phys. Chem. C* **2007**, *111*, 12243–12253.

(35) Koneracká, M.; Kopčanský, P.; Antalík, M.; Timko, M.; Ramchand, C. N.; Lobo, D.; Mehta, R. V.; Upadhyay, R. V. Immobilization of Proteins and Enzymes to Fine Magnetic Particles. *J. Magn. Magn. Mater.* **1999**, *201*, 427–430.

(36) Teranishi, T.; Miyake, M. Size Control of Palladium Nanoparticles and Their Crystal Structures. *Chem. Mater.* **1998**, *10*, 594–600.

(37) Li, R.; Zhang, P.; Huang, Y.; Zhang, P.; Zhong, H.; Chen, Q. Pd–Fe<sub>3</sub>O<sub>4</sub>@C Hybrid Nanoparticles: Preparation, Characterization, and Their High Catalytic Activity toward Suzuki Coupling Reactions. *J. Mater. Chem.* **2012**, *22*, 22750–22755.

(38) Ju, S.; Cai, T.-Y.; Lu, H.-S.; Gong, C.-D. Pressure-Induced Crystal Structure and Spin-State Transitions in Magnetite (Fe<sub>3</sub>O<sub>4</sub>). *J. Am. Chem. Soc.* **2012**, *134*, 13780–13786.

(39) de Rivera, F. G.; Angurell, I.; Rossell, M. D.; Ermi, R.; Llorca, J.; Divins, N. J.; Muller, G.; Seco, M.; Rossell, O. A General Approach To Fabricate Fe<sub>3</sub>O<sub>4</sub> Nanoparticles Decorated with Pd, Au, and Rh: Magnetically Recoverable and Reusable Catalysts for Suzuki C–C Cross-Coupling Reactions, Hydrogenation, and Sequential Reactions. *Chem. - Eur. J.* **2013**, *19*, 11963–11974.

(40) Erős, G.; Nagy, K.; Mehdi, H.; Pápai, I.; Nagy, P.; Király, P.; Tárkányi, G.; Soós, T. Catalytic Hydrogenation with Frustrated Lewis Pairs: Selectivity Achieved by Size-exclusion Design of Lewis Acids. *Chem. - Eur. J.* **2012**, *18*, 574–585.

(41) Sheldon, R. A.; Van Bekkum, H. *Fine Chemicals through Heterogeneous Catalysis*; John Wiley & Sons, 2008.

(42) Duan, Y.; Dong, X.; Song, T.; Wang, Z.; Xiao, J.; Yuan, Y.; Yang, Y. Hydrogenation of Functionalized Nitroarenes Catalyzed by Single-Phase Pyrite FeS<sub>2</sub> Nanoparticles on N,S-Codoped Porous Carbon. *ChemSusChem* **2019**, *12*, 4636–4644.

(43) Mohapatra, S. K.; Sonavane, S. U.; Jayaram, R. V.; Selvam, P. Regio- and Chemoselective Catalytic Transfer Hydrogenation of Aromatic Nitro and Carbonyl as Well as Reductive Cleavage of Azo Compounds over Novel Mesoporous NiMCM-41 Molecular Sieves. *Org. Lett.* **2002**, *4*, 4297–4300.

(44) Corma, A.; González-Arellano, C.; Iglesias, M.; Sánchez, F. Gold Complexes as Catalysts: Chemoselective Hydrogenation of Nitroarenes. *Appl. Catal., A* **2009**, *356*, 99–102.

(45) Makosch, M.; Sá, J.; Kartusch, C.; Richner, G.; van Bokhoven, J. A.; Hungerbühler, K. Hydrogenation of Nitrobenzene Over Au/MeOx Catalysts—A Matter of the Support. *ChemCatChem* **2012**, *4*, 59–63.

(46) Haber, F. On Electrolytically Precipitated Iron. *Z. Elektrochem. Angew. Phys. Chem.* **1898**, *4*, 506–514.

(47) Corma, A.; Concepción, P.; Serna, P. A Different Reaction Pathway for the Reduction of Aromatic Nitro Compounds on Gold Catalysts. *Angew. Chem.* **2007**, *119*, 7404–7407.

(48) Xuan, Q.; Song, Q. Diboron-Assisted Palladium-Catalyzed Transfer Hydrogenation of *N*-Heteroaromatics with Water as Hydrogen Donor and Solvent. *Org. Lett.* **2016**, *18*, 4250–4253.

(49) Cummings, S. P.; Le, T.-N.; Fernandez, G. E.; Quiambao, L. G.; Stokes, B. J. Tetrahydroxydiboron-Mediated Palladium-Catalyzed Transfer Hydrogenation and Deuteriation of Alkenes and Alkynes Using Water as the Stoichiometric H or D Atom Donor. *J. Am. Chem. Soc.* **2016**, *138*, 6107–6110.

(50) Kaur, R.; Kaur, G.; Gill, R. K.; Soni, R.; Bariwal, J. Recent Developments in Tubulin Polymerization Inhibitors: An Overview. *Eur. J. Med. Chem.* **2014**, *87*, 89–124.

(51) Tron, G. C.; Pirali, T.; Sorba, G.; Pagliai, F.; Busacca, S.; Genazzani, A. A. Medicinal Chemistry of Combretastatin A4: Present and Future Directions. *J. Med. Chem.* **2006**, *49*, 3033–3044.